

RESEARCH ARTICLE

10.1002/2015JB012431

Key Points:

- Steady state and transient postseismic fault creep in a thrust belt
- Nonlinear relationship between driving stress and creep rate
- Observations imply rate and/or state dependent fault friction

Correspondence to:

A. Copley,
acc41@cam.ac.uk

Citation:

Copley, A., and R. Jolivet (2016), Fault rheology in an aseismic fold-thrust belt (Shahdad, eastern Iran), *J. Geophys. Res. Solid Earth*, 121, doi:10.1002/2015JB012431.

Received 7 AUG 2015

Accepted 24 DEC 2015

Accepted article online 28 DEC 2015

Fault rheology in an aseismic fold-thrust belt (Shahdad, eastern Iran)

Alex Copley¹ and Romain Jolivet^{1,2}
¹COMET, Bullard Labs, Department of Earth Sciences, University of Cambridge, Cambridge, UK, ²Now at Laboratoire de Géologie, Département de Géosciences, École Normale Supérieure, PSL Research University, UMR CNRS 8538, Paris, France

Abstract Geodetic observations of aseismic deformation in a thrust belt near Shahdad in eastern Iran have been used to place constraints on the rheology of creeping faults in a thin-skinned thrust belt (<5 km thickness). Creep on shallow and high-angle thrust ramps at the range front occurs at a steady rate, in response to the topographic gradient across the thrust belt. Parts of these thrust ramps, and the low-angle basal thrust they connect to at depth in a ramp-and-flat geometry, underwent accelerated creep following the nearby M_w 6.6 Fandoqa earthquake in 1998. Estimates of the rate of fault slip and the driving stresses in these two contrasting times reveal a nonlinear relationship between the stresses and sliding velocity. The degree of nonlinearity rules out bulk shear of a weak layer in the sedimentary section (e.g., evaporites) as the deformation mechanism. Instead, we suggest that the motions are accommodated by slip on faults governed by a friction law with a highly nonlinear relationship between shear stress and slip rate (e.g., as predicted by “rate and state” models). The high-angle thrust ramps are responsible for building aspects of the geological and geomorphological signs of active shortening visible at the surface, but the folding preserved in the geology must be accomplished by other methods, possibly during the rapid transient postseismic deformation following nearby earthquakes.

1. Introduction

Numerous observations from a range of tectonic settings have highlighted the spatial variability in fault deformation style, from segments remaining locked in the interseismic period and subsequently breaking in earthquakes, to others undergoing inter-earthquake and post-earthquake aseismic sliding. To fully understand this range of behavior, and other fault slip phenomena such as tremor and slow-slip events, requires knowledge of the rheological laws that control the evolution of stress and displacement on faults. A popular approach is based upon laboratory experiments and is the “rate-and-state friction” formulation [e.g., *Dietrich*, 1979; *Ruina*, 1983; *Marone*, 1998], in which the effective coefficient of friction of a fault depends upon the rate of sliding and the evolution through slip of a state variable (which describes changes in the structural properties of the fault, such as the time over which asperities have been in contact). This friction law has been used to reproduce a range of fault slip observations, largely based upon the difference between stick slip and creeping patches of faults, and transient deformation in the postseismic period [e.g., *Scholz*, 1998; *Hearn et al.*, 2002; *Perfettini and Avouac*, 2004; *Johnson et al.*, 2006; *Barbot et al.*, 2009; *Copley et al.*, 2012; *Kaneko et al.*, 2013]. However, the geometrical and temporal simplicity of observed fault slip patterns, and the difficulties in estimating the absolute stresses exerted on the faults (as distinct from the stress changes due to earthquakes), make it difficult to test in which natural systems rate-and-state friction laws may apply. This paper uses pre-seismic, coseismic, and postseismic interferometric synthetic aperture radar (InSAR) observations to study the thrust belt flanking the fault that ruptured in the 1998 M_w 6.6 Fandoqa earthquake in eastern Iran. Using these observations, it is possible to test what rheologies are consistent with the evolution of fault displacements through time, in a region where the absolute magnitude of tectonic forcing can be estimated.

The 14 March 1998 M_w 6.6 Fandoqa earthquake was an oblique right-lateral strike-slip event, with a normal-faulting component of motion, on a plane dipping WSW at 50° in the Gowk fault zone in eastern Iran (Figure 1a) [*Berberian et al.*, 2001]. SAR interferograms spanning the earthquake and the subsequent 6 months revealed a signal that could be modeled by ~8 cm of motion on a low-angle thrust plane underlying the adjacent Shahdad thrust belt, in a region where the stress changes due to the earthquake promoted thrust motion [*Berberian et al.*, 2001; *Fielding et al.*, 2004] (Figure 1c). This motion is thought to be postseismic creep because

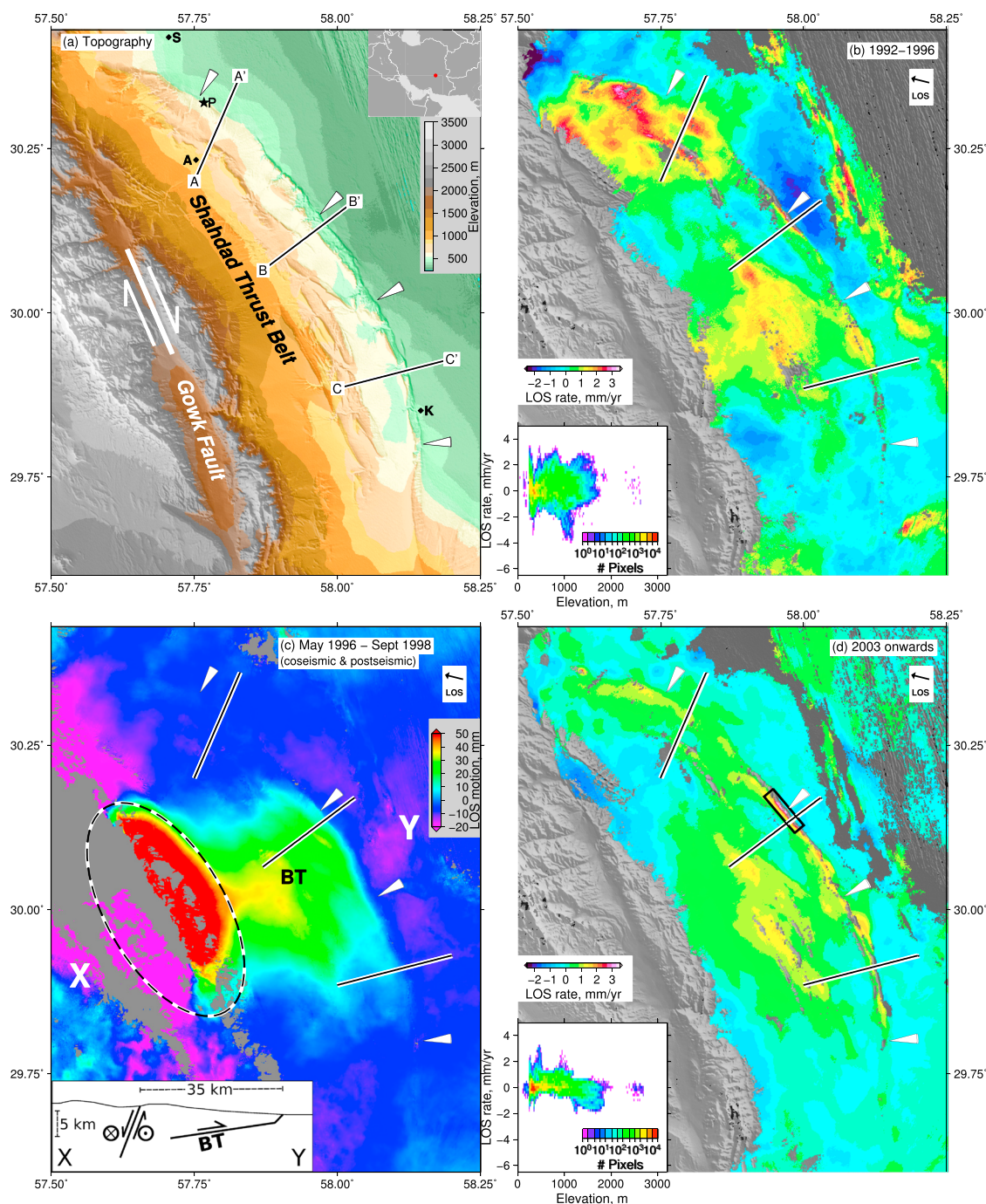


Figure 1. (a) Topography in the region of the Gowk Fault and Shahdad thrust belt, illuminated from the southwest. The inset shows the location within Iran. The white line shows the fault rupture of the 1998 Fandoqa earthquake on the Gowk Fault. To aid comparison between figures, the same four locations on the thrust range front are marked by white arrows on all panels. S, A, and K show the settlements of Shahdad, Andoujherd, and Keshit. P shows the location of the photographs in Figure 6. (b) Stack of interferogram spanning 1992–1996, shown as solid lines in Figure 2. In Figures 1b–1d, the satellite line of sight is inclined at 23° from the vertical, and in the direction shown by the black arrow marked “LOS.” In all figures positive values correspond to motion toward the satellite. Inset shows the lack of relationship between elevation and apparent rate of ground motion. (c) Interferogram covering May 1996–September 1998 (previously studied by Berberian *et al.* [2001] and Fielding *et al.* [2004]), expressed as ground motion in the satellite line of sight (LOS). The displacements due to the Fandoqa earthquake (on 14 March 1998) are saturated on this color scale and are in the area shown by the dashed ellipse. The surface motions due to slip on a low-angle thrust underlying the Shahdad thrust belt are marked “BT” (Basal Thrust) and are represented by the lobe of ground motions of up to 35 mm, to the NE of the Fandoqa event. Inset shows a schematic diagram of the fault motion on the high-angle Gowk fault and low-angle basal thrust in the time period covered by the interferogram (from Berberian *et al.* [2001] and Fielding *et al.* [2004]). (d) Stack of interferograms spanning 2003–2009, shown as solid lines in Figure 2. Inset shows the lack of relationship between elevation and apparent rate of ground motion.

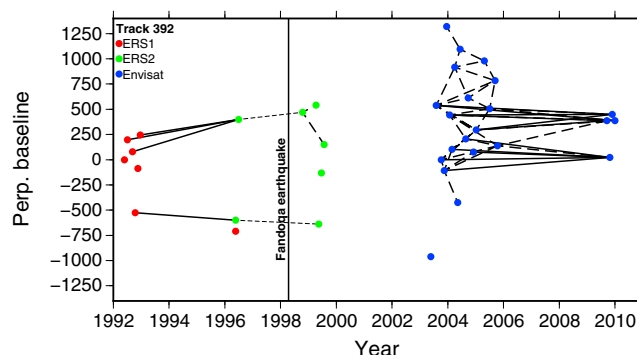


Figure 2. The available SAR acquisitions from descending track 392, color coded by satellite. Solid lines show interferograms included in the stacks shown in Figure 1. Thin dashed lines covering 1996–1998 show the interferograms covering the Fandoqa earthquake and initial postseismic period, as studied by *Berberian et al.* [2001] and *Fielding et al.* [2004] (with the upper one shown in Figure 1c). The dashed lines linking Envisat acquisitions show the interferograms that, along with those shown as solid lines, were used to produce the time series of displacements in Figure 4. The dashed lines linking postseismic ERS2 acquisitions show some interferograms which limit the time span of rapid postseismic motions, as discussed in the text.

the displacement-to-length ratio of slip on the fault was significantly outside the range observed for earthquakes. This low-angle plane that underlies the thrust belt will be referred to in the remainder of the paper as the “basal thrust.” This paper uses InSAR to examine the motions in the decade following the time interval studied by *Berberian et al.* [2001] and *Fielding et al.* [2004], and also in the time preceding the earthquake. By combining these observations with the results of *Berberian et al.* [2001] and *Fielding et al.* [2004], and with a model for the forces being exerted on the thrust belt, it is possible to infer some aspects of the rheology of the shallow, creeping faults in the region. It is also possible to examine how fault slip contributes to the growth of geological and topographic structures.

2. InSAR Observations

Figure 1 shows the topography of the Gowk Fault and the Shahdad thrust belt, along with InSAR results from three different time periods. Figure 1b shows a stack of four descending track interferograms from the period before the earthquake, with a cumulative observation time of 14.3 years (details of all the interferograms used in this study are given in Table A1 in Appendix A). The SAR interferograms used are shown as solid lines in the period 1992–1996 in Figure 2. These represent all of the multiyear pre-earthquake interferograms that are not incoherent in areas of interest (due to large perpendicular baselines) or affected by large turbulent atmospheric effects (as is the case with those constructed using the SAR scene from 21 April 1996). Figure 1c shows an interferogram covering the time of the Fandoqa earthquake, along with approximately 2 years before the earthquake and 6 months after the event. This interferogram, shown by the upper thin dashed line in Figure 2, was also studied by *Berberian et al.* [2001] and *Fielding et al.* [2004]. Figure 1d shows a stack of 11 descending track interferograms covering a cumulative observation time of 61.5 years from the period 2003–2009, shown as solid lines in Figure 2. These interferograms were selected because they have short perpendicular baselines and long time spans. The other possible interferograms were not included at this stage in order to preserve coherence as much as possible, but will be analyzed below. Maps of the standard deviations in both stacks of interferograms are shown in Appendix A. Figure 3 shows profiles through the topography and the three periods of geodetic results along the lines marked in Figure 1. Our InSAR results span a range of pre-earthquake, co-earthquake, and post-earthquake deformation.

The interferogram covering the earthquake and the subsequent 6 months (Figure 1c) was studied by *Berberian et al.* [2001] and *Fielding et al.* [2004] and represents the slip in the Fandoqa earthquake on the Gowk Fault (dashed oval in Figure 1b) plus sliding on the basal thrust underlying the Shahdad thrust belt (the wide lobe to the NE of the earthquake, showing 20–35 mm of satellite line-of-sight motion, marked “BT”). The inset in Figure 1c schematically shows the fault motion during this time period.

The stacks of interferograms covering 1992–1996 and 2003–2009 show patterns that are similar to each other, but different to those covering the earthquake and the early postseismic deformation. Both stacks of

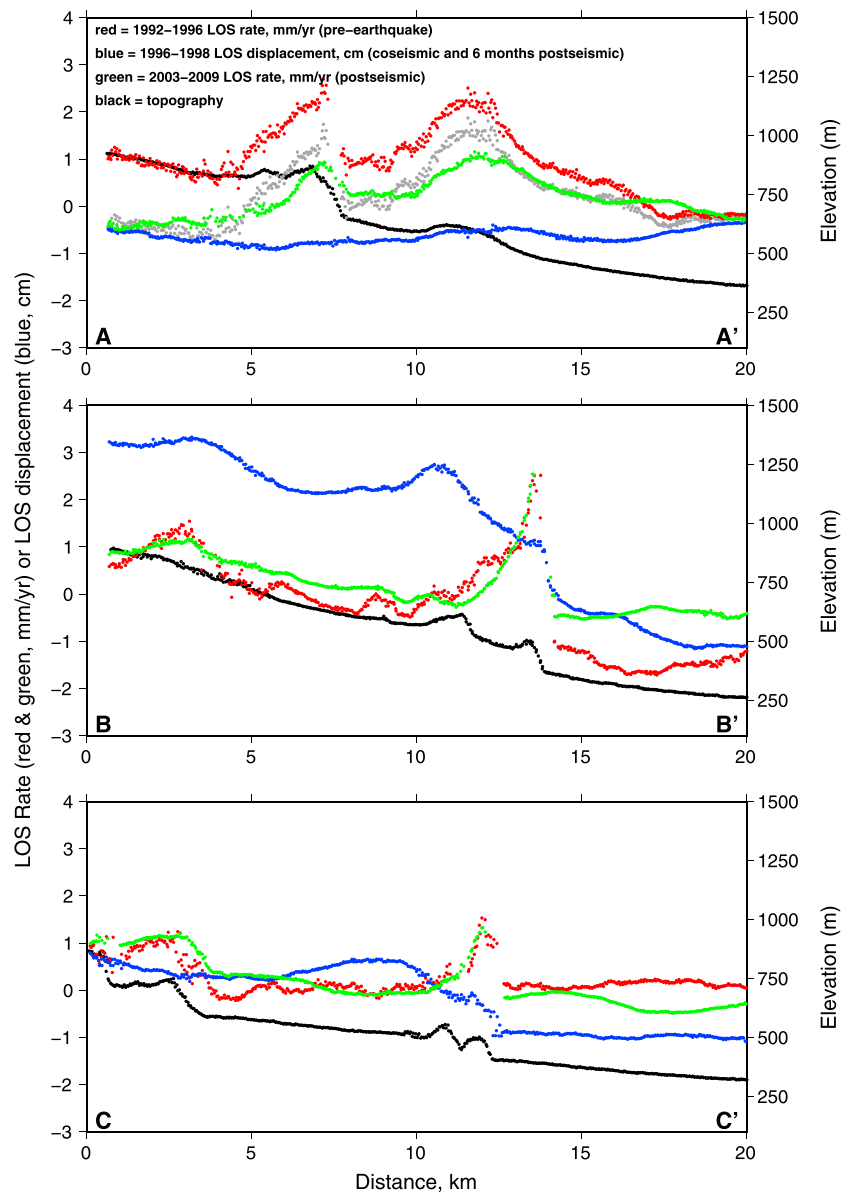


Figure 3. Profiles along the lines labelled in Figure 1 of topography (black), average rate of line-of-sight motion (in mm/yr; red: 1992–1996; and green: 2003–2009) and displacement from 1996–1998 (in cm; blue). The grey points on profile A–A' show the red points after the removal of a linear trend from the profile (such as could result, for example, from long-wavelength atmospheric effects).

interferograms show an arc of deformation following the outer edge of the thrust belt at time-averaged rates of 1.5–3.5 mm/yr. Both also show a signal in the belt interior, in the same location as the signal marked BT in Figure 1c. There are other signals present in the pre-earthquake stack that are not in the post-earthquake results. Some of these signals are likely to represent nontectonic motions (e.g., in the area of sand dunes to the east of the thrust belt). Others could be tectonic motion (e.g., the large area of apparent motion toward the satellite in the northern part of the interior of the thrust belt), but the limited number of usable SAR acquisitions in 1996 makes the interpretation of these signals problematic, as they only appear on some interferograms. We focus on the signals that appear on all interferograms, which are the arc of deformation on the margin of the thrust belt, and the motions in the interior of the belt in the same location as the signal marked BT in Figure 1c.

A number of observations suggest that the arc of deformation on the edge of the thrust belt represents tectonic ground motion. First, the insets in Figures 1b and 1d show that the apparent line-of-sight motion is

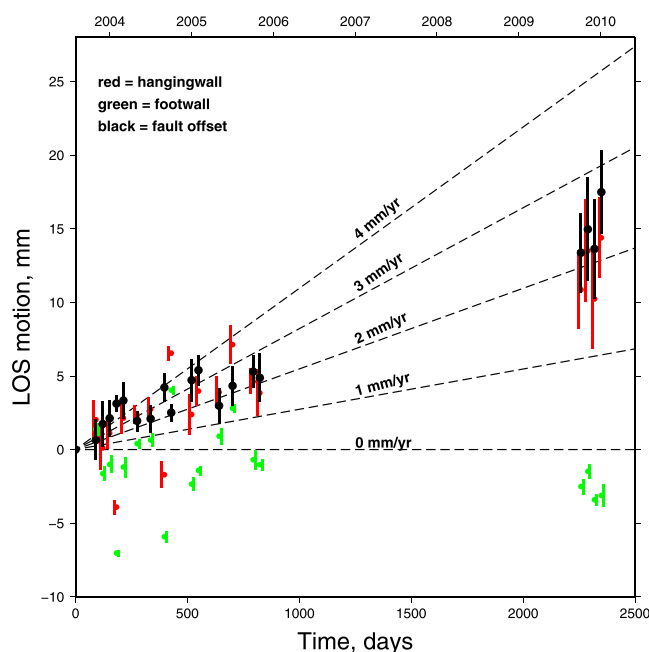


Figure 4. Time series of line-of-sight displacements relative to the SAR acquisition on 6 June 2003. Measurements are averaged in the area of the black box in Figure 1d. Red points represent the hanging wall side of the fault, green the footwall, and black the offset between them.

independent of elevation on both stacks, ruling out topographically correlated atmospheric effects as a source of the signals. Second, the signal evolves in a steady manner through time, with longer-timespan interferograms showing larger amounts of ground motion (discussed in more detail below). Such a clear relationship would not be expected for other potential sources of InSAR signals. Third, the signal is visible on all interferograms, produced using a range of independent data acquisitions, and shows no relationship to interferometric baseline. Finally, the shape of the signals (discussed in more detail below), the lack of correlation between signal size and the time of year of the SAR acquisitions, the absence of the signal from the geologically and climatically similar regions along-strike of Shahdad, and the arid climate of the area suggest that the motions are not due to aquifer filling and discharge.

The sharp discontinuities in the ground motion signal (Figures 1 and 3) imply that the deformation is the result of slip on faults that break the surface and underlie the margin of the fold-thrust belt. In addition to those signals, there is also some suggestion that the basal thrust motion seen in the interferogram covering the coseismic and the first 6 months of the postseismic period may both predate and postdate the earthquake, with a rate of line-of-sight motion of ~ 1 – 1.5 mm/yr (yellow area in the center of the fold belt in Figures 1b and 1d, in the location marked “BT” in Figure 1c). These signals will be discussed in more detail below.

We also computed and analyzed ascending track interferograms. The interferograms, and stack of all the results, show a clear correlation between elevation and phase, suggesting the signal is dominated by topographically correlated atmospheric effects (see Appendix B). The apparent motion within the thrust belt due to these effects overwhelms the ground motion signals visible in the descending track data that we discuss above. This effect is exacerbated by the geometry of the faulting (described in more detail below) leading to smaller signals in ascending track data than descending track results by a factor of ~ 2 . An analysis of the time series of displacements was unable to extract the ground motion effects from the atmospheric noise, due to the low signal-to-noise ratio. A full description is given in Appendix B. The contrast with the descending track data is likely to be due to the late afternoon data acquisition time, in contrast to the early morning descending track acquisitions. The ascending track data are consistent with the descending track results we discuss here, in the sense that the expected signal lies within the noise in the ascending track data. However, the signal is too small compared with the atmospheric effects to isolate, including if the methods of Jolivet *et al.* [2014] are utilized. We therefore do not consider the ascending track data any further in this study.

3. Temporal Evolution of Deformation

The available post-earthquake SAR data acquisitions have large gaps in 1998–2003 and 2005–2009 (Figure 2), limiting our ability to analyze how the motions vary through time. However, we have analyzed the temporal evolution of motions from 2003 onward. We have constructed all of the interferograms shown by dashed lines linking Envisat data acquisitions in Figure 2, in addition to those shown by solid lines used in the stacks described above. We have then performed a least squares inversion to estimate the evolution through time of the deformation [e.g., Usai, 2003]. This procedure used 48 interferograms and obtained estimates for the displacement at each of 21 Envisat acquisition dates. Figure 4 shows the results from inside the black box marked in Figure 1d, where profile B–B' crosses the range front. Both sides of the fault show similar apparent motion due to atmospheric signals. However, the offset between locations on the footwall (green points) and hanging wall (red points) sides of the fault increases with time (shown by black points). The data are consistent with the fault motion trend being linear, and given the errors in the data and the temporal gap in the SAR acquisitions a more complex view of the evolution through time is not warranted. The average rate of motion within the box (2–3 mm/yr) is, within error, the same as the average preseismic rate in the same location (Figure 1b).

The short time period ERS2 interferograms covering 1998–1999 show small offsets in phase at the range front of the thrust belt. Although these measurements are consistent with the rates estimated for the 1992–1996 and 2003–2009 time periods, they are not robust because the signals are small, and there are only two available interferograms. However, it is possible to conclude that the rapid transient motions that occurred following the Fandoqa earthquake (Figure 1c) had decayed away by the time of the 1998–1999 interferograms.

In summary, motion occurred with a similar rate and geometry in the periods before and significantly after the Fandoqa earthquake (Figures 1b, 1d, and 4), and this motion was interrupted by a period of rapid transient deformation, caused by the Fandoqa event, that lasted for 6 months or less (Figure 1c). We discuss the mechanical implications of this behavior below.

4. Models of Fault Slip

In the remainder of this paper we focus our attention on the range-bounding thrust in the location of the black box in Figure 1d, where profile B–B' crosses the range front. This fault was slipping in all time periods covered by our InSAR data and so provides an opportunity to probe the rheology of the fault by examining how it responded to the stress changes from the Fandoqa earthquake. The sharp discontinuity in ground motion due to the fault reaching the surface makes the interpretation of the signal less ambiguous than those from deeper sources.

To analyze the observed ground motions in the period from 2003 to 2009, inversions have been performed on a profile through an interferogram covering June 2003 to October 2009 (shown in Appendix C). This interferogram was used, rather than the stacks of data, in order to take advantage of the higher coherence in the individual interferogram. We model the displacements along a profile, rather than the full two-dimensional surface displacement field, because long-wavelength nontectonic signals in the interferograms make modeling the full displacement field problematic. We assume that the surface motions are exclusively due to fault motions and longer-wavelength noise in the data. In common with most geodetic studies of fault slip, our neglect of anelastic deformation in the material surrounding the fault could affect the details of our estimated parameters.

The results of the inversion for fault slip on profile B–B' are shown in Figure 5. A grid search has been used, along with a model for uniform slip on a rectangular plane in an elastic half-space [Okada, 1985], to find the best fit to the data by varying seven parameters: the fault location along the profile, the dip, top depth, bottom depth, and slip rate, plus an offset of the data relative to zero and a gradient along the profile (in order to account for nontectonic signals such as orbital residuals and long-wavelength atmospheric effects). The fault is assumed to slip in a pure thrust sense, and the strike and along-strike length of the fault segment were fixed based upon the expression of the fault in the geomorphology. Figure 5 shows the best fit model and the range of fault parameters that can fit the data to within 25% of the best fitting solution. These inversions show that the fault has a steep dip ($55^\circ \pm 10^\circ$), reaches from the surface to a depth of 1.0 to 1.5 km and slips at 6.5 ± 1.5 mm/yr. The depth to the base of the fault is similar to the estimated depth of the basal

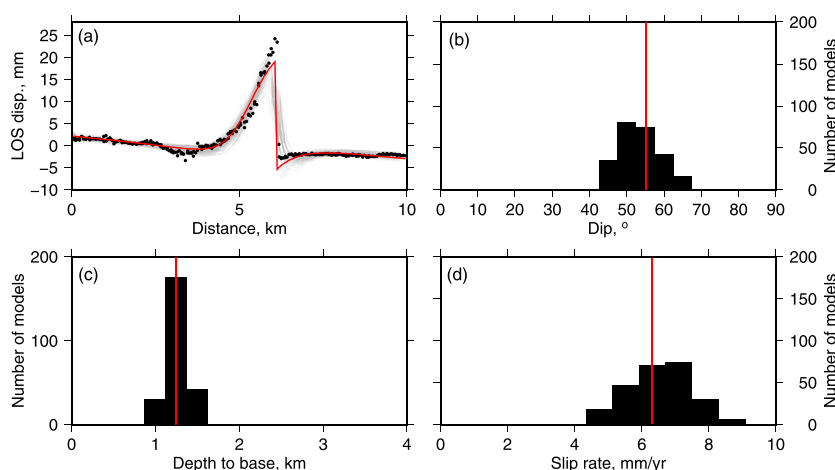


Figure 5. (a) Black circles are displacements in the InSAR line of sight from an interferogram covering June 2003 to October 2009 (shown in Appendix C), along the line of profile B–B' shown in Figure 1a. Red line is the best fitting model due to slip on a fault, and grey lines are models that fit the data to within 25% of the minimum misfit. (b) Dips of the faults that fit the data to within 25% of the minimum misfit solution. The red line shows the best fit solution. (c and d) As Figure 5b, but for the depth to the base of the fault and the amount of slip (expressed as the average slip rate over the time interval covered by the interferogram). The fault strike and along-strike length were taken as 50° and 5 km.

thrust underlying the thrust belt, if projected to the range front [Berberian *et al.*, 2001; Fielding *et al.*, 2004]. However, the dip of the fault studied here is much steeper than that of the basal thrust (which dips at ~6°). These results suggest that the range front fault represents the steep ramp at the nose of a ramp-and-flat thrust system, with the basal thrust that moved following the Fandoqa earthquake representing the “flat” section. Models of the displacements on profiles A–A' and C–C' (shown in Appendix C) show similar patterns. The fault crossed by profile C–C' (Figure 1) slips at 4 ± 1 mm/yr from the surface to a depth of 1.25–1.75 km on a fault dipping at 50–65°. The fault crossed by profile A–A' does not reach the surface, creating a smoother displacement pattern and resulting in larger trade-offs between model parameters. The fault top is at a depth of 1–3 km and the base at 2.5–4.5 km. The dip could be into or out of the range and is probably in the range 40°–60°, but could be as low as 20°. The slip rate is likely to be 2–6 mm/yr but could be up to 8 mm/yr (see Appendix C).

In the models above, the displacement peak at the thrust range front was analyzed, and we solved for an offset of the data relative to zero and a gradient along the profile. In this situation, the inversion methodology is insensitive to slip on a gently dipping basal thrust connecting to the base of the higher-angle thrust ramps at the range front. Such motion would be expected to be present, to accommodate the motion on the thrust ramp. If basal thrust slip were present at the same rate as motion on the thrust front, then a line-of-sight velocity of 1–2 mm/yr would be expected in the center of the thrust belt. The stacks of interferograms shown in Figures 1b and 1d suggest that such motions may be present. However, the standard deviation maps in Appendix A show values of 1–1.5 mm/yr in this region, similar in magnitude to the expected signals (and note that these maps do not represent errors that are common to all interferograms in the stacks). Our interpretation is therefore limited to noting that the signals in the belt interior in Figures 1b and 1d are consistent with basal slip at rates of 5 ± 2 mm/yr (estimated using the same fault geometry as the distributed-slip inversions of Fielding *et al.* [2004]). Such slip is sufficient to accommodate the motion on the range front thrust ramps, but errors in the data mean that this estimate is imprecise. Due to the low signal-to-noise ratio in the belt interior, we instead concentrate our attention on the clearer signal at the thrust front. We also note that there appear to be fault strands reaching the surface in the center of the thrust belt that have been active at all time periods covered by our InSAR data (visible as discontinuities in Figure 1). However, due to the much greater rates of motion, and therefore higher signal-to-noise ratio, we focus in the remainder of the paper on the more rapidly slipping range-bounding faults. Our results presented below regarding the range front thrust are independent of the interpretation of the signal in the range interior.

The total moment release implied by the post-earthquake InSAR results is equivalent to $\sim 4 \times 10^{16}$ Nm/yr, summed over the entire range front of the thrust belt (assuming a slip rate of 5 mm/yr along the 100 km

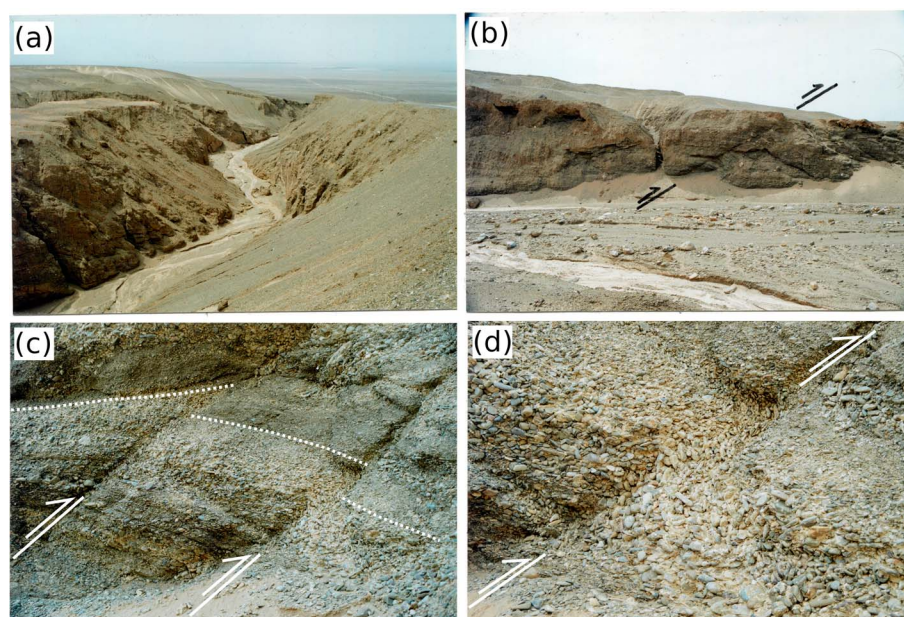


Figure 6. (a) View looking to the northeast from the interior of the thrust belt toward the range front, in the location marked “P” in Figure 1 ($30^{\circ}19.16'N$, $57^{\circ}46.01'E$). Note the tilted beds in the middle distance that form part of an anticline. (b) Fault cutting alluvial gravels near the range front in the river valley pictured in Figure 6a. (c) Multiple faults cutting alluvial gravels near the range front in the river valley pictured in Figure 6a. The top of a distinctive pale layer is marked by a dotted white line. (d) Detail of the thrust offset of the pale gravels on the right-hand fault in Figure 6c. Photographs courtesy of James Jackson.

margin of the thrust belt, from the surface to a depth of 1.5 km on faults dipping at 55° , and a shear modulus of 4×10^{10} Pa). In the time interval from 2003 onward, which is the time period covered by the interferograms in the descending track stack of data, the largest earthquakes in the region of the thrust belt were five events of M_b 3.4–3.7 (equivalent to a rate of moment release of $<2 \times 10^{14}$ Nm/yr). This comparison suggests the deformation observed with InSAR was dominantly aseismic. The lack of major aftershocks in the region of the Shahdad thrust belt following the Fandoqa earthquake, and the presence of the fault creep discussed here, suggests a fault rheology in the thrust belt that is unable to generate significant earthquakes.

5. Comparison to Geomorphology and Geology

It is possible to estimate the horizontal length scale of active uplift at the range front using the distance over which rivers incise deep gorges, and the locations of outcrops of rocks that have been exhumed by faulting and/or folding [e.g., Walker and Jackson, 2002]. At the thrust front, this length scale (1.5–3.5 km) closely matches that produced by the motion on the steep range front thrust ramps, as observed in the InSAR results. The width of the zone of river incision is larger in the northern part of the thrust belt than in the central and southern parts (up to 6 km), consistent with the deeper faulting and wider surface deformation signal seen on profile A–A'. This observation implies that, along with two other thrust belts in east Iran that have been studied using similar methods [Copley, 2014; Copley and Reynolds, 2014], the aseismic fault creep has played a role in creating shallow geological and geomorphological structures. Such deformation provides an explanation for the construction of short-wavelength topographic and geological structures: unlike in an elastic-rebound earthquake cycle, the fault slip is not balanced by prior elastic strain buildup, thereby allowing the production of short-wavelength finite strain adjacent to faults.

If the apparent variations of line-of-sight motions within the interior of the thrust belt seen in Figure 1 are real, and not atmospheric artifacts, then there may be transient elastic strain accumulation present. It is also possible that the upper 1–3 km of the crust on profile A–A' is accumulating elastic strain. Alternatively, these surface motion variations may record distributed permanent deformation. However, these features are of second order compared with the direct correspondence between the length scale of uplift seen in the geology and geomorphology, and the location of rapid range front uplift due to fault creep observed by InSAR.

Figure 6 shows a photograph of the interior of the thrust belt at the location marked “P” in Figure 1, and close-up views of faulting within the alluvial gravels that are being uplifted near the range front. Multiple faults within the gravels offset the sedimentary layering and dip at angles consistent with the inversions for the dip of the range front faults described above. The fieldwork was undertaken by James Jackson and colleagues from the Geological Survey of Iran in 1998, following the Fandoqa earthquake, so it was not possible at that time to try and relate the faults visible in the field with the InSAR results presented here (which postdate the fieldwork). The presence of folded beds (Figure 6a) raises the question of when in the earthquake cycle these features are produced. The motions from late 1998 onward appear to be dominated by slip on faults, rather than distributed folding. There are three options for when the folding may be occurring. First, it could happen in response to a driving stress that was not present during the period covered by the SAR data studied here (e.g., an earthquake on a structure other than the Gowk Fault). Second, the motion could occur continuously at a slow enough rate to not be visible. Third, in the interferogram that covers the Fandoqa earthquake and the first 6 months of the postseismic period, the profiles B–B’ and C–C’ in Figure 1 show significant gradients in the ground motion in addition to the sharp step at the range front (e.g., at ~11–14 km along profile B–B’ in Figure 3). These gradients could represent elastic strains generated by variations in slip on the underlying basal thrust, or could be caused by permanent deformation and distributed folding. Although our available information does not allow us to distinguish between these options, it is possible that the folding happens during the relatively rapid deformation following nearby earthquakes that impose stress on the fold belt. An analogous situation exists in the Tabas fold-thrust belt in eastern Iran, where active folding by bedding-plane slip happened during the 1978 M_w 7.3 thrust earthquake, and shallow fault creep in the same anticlines occurred during the subsequent slower postseismic deformation [Berberian, 1979; Walker et al., 2003; Copley, 2014].

The rates of fault creep that we estimate above would generate significant topography over million year timescales (e.g., ~5 km over 1 Ma). The absence of such a high mountain range at Shahdad is likely to be due to a combination of factors. The location of thrust motion is thought to have changed through time (migrating outward toward the basin) [i.e., Walker and Jackson, 2002]. Erosion of material from the thrust belt and redeposition in the Lut desert is observed at the present day and presumably also happened in the past. Finally, the rate of fault motion may have changed on million year timescales in response to gravity acting upon a thrust belt with an evolving distribution of elevation (see section 7 for a discussion of the role of gravitational forces in driving the present-day deformation).

6. Comparing Rates of Deformation

The results presented above have shown that there was slip on the range front fault in the period before the Fandoqa earthquake (Figure 1b), and a similar rate and geometry of slip in the period from 2003 onward, significantly after the earthquake (Figure 1d). The previous results of Berberian et al. [2001] and Fielding et al. [2004] show that much more rapid fault motion occurred in the 6 months following the Fandoqa event, shown by the range front step in the blue line in Figure 3b. This motion represents an average line-of-sight displacement of ~5.2 mm/yr at the range front on profile B–B’, which is significantly higher than the 2–3.5 mm/yr average estimated during the pre-earthquake and late post-earthquake periods (Figure 4). As discussed below, if this increase in average rate was due to transient postseismic slip immediately following the Fandoqa earthquake, then this transient slip rate was on the order of tens of millimeters per year. The motions on the range front in the central part of the thrust belt therefore represent ongoing aseismic creep, punctuated by a phase of rapid motion triggered by stress changes from the nearby Fandoqa event. In the remainder of this paper the fault motion occurring before, and significantly after, the Fandoqa earthquake will be referred to as “steady state” creep, although it should be noted that variations in creep rate over longer or shorter timescales than sampled by the SAR data cannot be ruled out.

Because there are no SAR acquisitions immediately after the Fandoqa earthquake, it is not known for certain that the motion in the Shahdad thrust belt in the period 1996–1998 was postseismic, rather than coseismic. However, following Berberian et al. [2001] and Fielding et al. [2004], we believe that the ratio of displacement to length on the slip patch beneath the thrust belt, which is an order of magnitude lower than seen in earthquakes, suggests that the motions represent postseismic sliding. In addition, it seems unlikely that seismic slip from the Fandoqa earthquake (with a ~20 km long fault plane) dynamically propagated for ~35 km on a fault off the main shock fault plane, producing only ~8 cm of slip. We therefore assume that the motions were postseismic, but note that any coseismic contribution to the slip would reduce our estimated rates of postseismic motion that are discussed below.

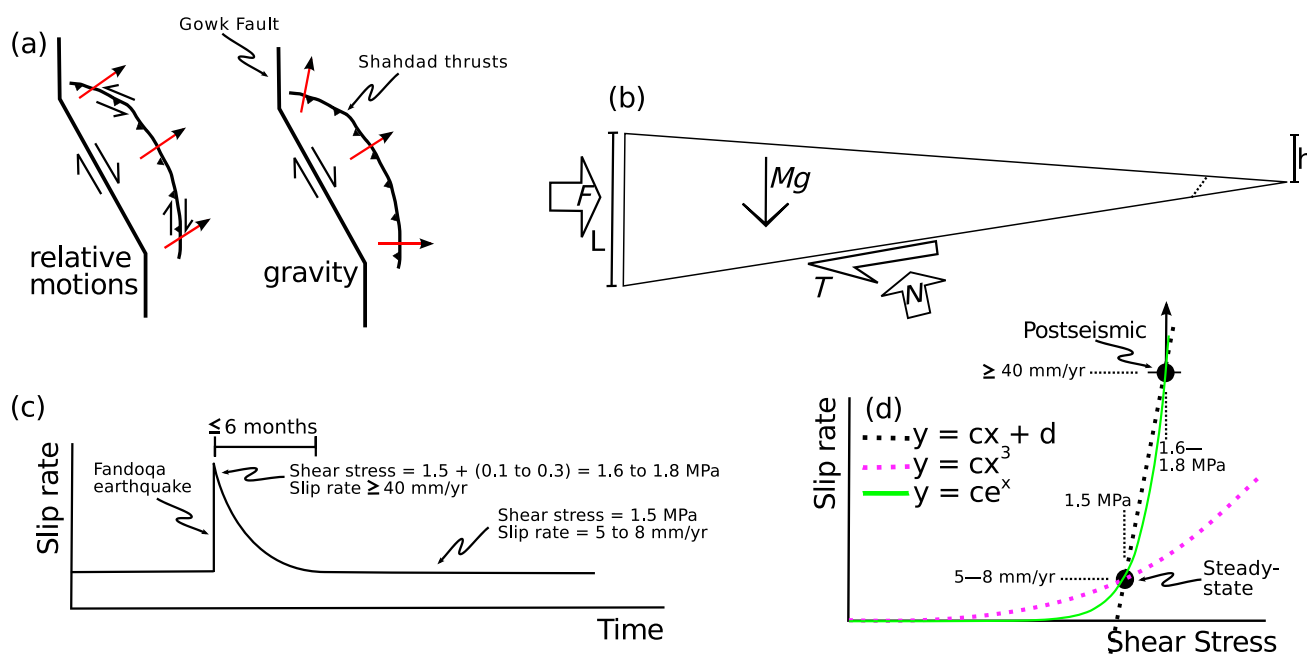


Figure 7. (a) Schematic pattern of deformation in the Shahdad thrust belt depending on whether the motions are governed by the relative motions of the bounding crustal blocks or by gravitational driving forces. (b) Balance of forces on the thrust wedge. For simplicity, the change in dip at the nose of the wedge (dotted line) is neglected. See text for discussion of the magnitudes of the forces. (c) Schematic pattern of slip rate through time for the Shahdad thrust system and the calculated shear stresses on the faults. (d) Relationship between shear stress and slip rate for the Shahdad thrust faults, along with curves drawn using a range of functional forms. See text for details.

Results from regional GPS observations suggest that the rate of horizontal shortening on the Shahdad thrust belt is ~ 3 mm/yr [Walpersdorf *et al.*, 2014]. The motions we have observed with InSAR in the periods before 1996 and after 2003 suggest horizontal shortening of 2–5 mm/yr, depending on the fault dip and rate of motion (Figure 5). This comparison implies that the motion we have imaged by InSAR during these times represents creep at close to the time-averaged rate of shortening (particularly once the effects of gravitational driving forces are taken into account, as described below).

7. Driving Stresses

The presence on the Shahdad thrust range front of both rapid fault creep following the Fandoqa earthquake [Berberian *et al.*, 2001; Fielding *et al.*, 2004], and slower steady state creep, provides a means to probe the rheology of the faults. To do so requires calculations of the stresses driving both the steady state and postseismic transient creep, and estimates of the rate of fault motion at these two times.

The stress changes on the surrounding faults due to the Fandoqa earthquake and the slip on the basal thrust can be calculated using the slip model of Fielding *et al.* [2004] and the fault geometry estimated in Figure 5. On the range front fault at the location of the black box in Figure 1d, the stress change involves an increase in shear stress of 0.2–0.3 MPa in a thrust-faulting sense, and an increase in the normal stress of 0.1–0.2 MPa. The coulomb stress change is therefore 0.1–0.3 MPa, for coefficients of friction of 0.1–0.6.

The maximum rate of fault slip on the range front thrust ramp in the immediate postseismic period following the Fandoqa earthquake is difficult to estimate without knowledge of the temporal evolution of the transient slip, which is not possible with the available SAR data. However, a minimum bound can be calculated using the total motion where the thrust ramp reaches the surface on profile B–B' in the interferogram covering May 1996–September 1998. The rate of steady state creep discussed above can be used to estimate the amount of line-of-sight motion between the start date of the interferogram and the Fandoqa earthquake in March 1998 (3.6–6.3 mm, for preseismic rates of 2.0–3.5 mm/yr). The remainder of the total line-of-sight motion at the range front on profile B–B' can then be estimated (5.7–8.4 mm). A lower bound on the maximum postseismic line-of-sight rate can be calculated by assuming that this motion occurred at a linearly

decreasing rate throughout the remainder of the time covered by the interferogram, and is 23–34 mm/yr. Using the fault geometry shown in Figure 5, this line-of-sight rate can be converted into a fault slip rate of 41–60 mm/yr. This estimate would be increased if the decay in slip rate was not linear, but faster earlier in the postseismic period (as often observed), or if the transient deformation occurred over less than the 6 months of the postseismic period sampled by this interferogram.

The rate of steady state fault creep has been estimated above, from the models of the InSAR results, and is 5–8 mm/yr. To estimate the stresses driving this deformation, we need to establish the governing driving forces. The Shahdad thrust belt occurs at a restraining bend in the strike-slip faults that run along the western side of the Lut desert. The component of shortening across this restraining bend has resulted in the construction of the thrust belt. As a thrust belt increases in elevation, the forces due to gravity acting on elevation contrasts also increase and can begin to play a role in controlling the deformation. Shortening occurs perpendicular to the strike of the curved edge of the Shahdad thrust belt around the entire margin of the range [e.g., *Geological Survey of Iran*, 1992, 1993; *Walker and Jackson*, 2002], with no evidence of significant strike-slip faulting in the region to the NE of the Gowk Fault. This configuration implies that the thrust belt has reached a high enough elevation that gravitational driving forces have become important in controlling the deformation. Such forces result in shortening perpendicular to the local strike of the range (e.g., as observed in southern Tibet and the Sulaiman fold-thrust belt [Copley and McKenzie, 2007; Reynolds et al., 2015] and shown schematically in Figure 7a), and the generation curved margins to thrust belts [e.g., Copley, 2012], as are seen at Shahdad. If only the relative motion across the fault system were important, given by the velocities of the bounding crustal blocks, then one or both of the margins of such a curved thrust belt (with a 70° change in strike between the northern and southern ends) should be characterized by strike-slip motion, rather than the folding and thrust faulting visible in the Neogene geology [e.g., *Geological Survey of Iran*, 1992, 1993; *Walker and Jackson*, 2002].

It is possible to estimate the magnitude of the stresses driving the steady state creep by balancing the forces acting on the thrust belt (Figure 7b). It is convenient to make the simplifying assumption of ignoring the change in fault dip at the toe of the wedge, which has little effect on the calculations. The stresses on the wedge are the normal stresses and shear tractions on the faults (N and T in Figure 7b), gravity acting upon the rocks in the thrust belt (Mg), and the stresses imposed on the rear, high elevation, end of the wedge (F). Because of the likely importance of gravitational forces in controlling the deformation, the total force on the back of the wedge (F in Figure 7b) has been set to be equal to the depth integral of the lithostatic pressure (i.e., there is no significant force being exerted on the back of the wedge beyond that related to the surface elevation). This quantity is given by $\rho g L^2 / 2$, where ρ is the density, g is the acceleration due to gravity, and L is thickness of the thrust wedge as defined in Figure 7b. If we resolve forces parallel to the fault, taking the elevation difference over the thrust belt to be 1 km, the thickness at the back of the wedge to be 4 km, and the basal dip to be 6° [Berberian et al., 2001], then following the method of Lamb [2006] we can estimate the basal shear stress to be 1.5 MPa. This value is equivalent to an effective coefficient of friction of 0.01–0.06 for thrust depths of 1–5 km, similar to suggestions for thrust belts elsewhere [e.g., Suppe, 2007; Herman et al., 2010]. The shear stresses we estimate for the fault could be increased if there was a deviatoric compressive stress exerted on the back of the wedge or decreased if such a stress were extensional (i.e., if our inference of the dominance of gravitational driving forces were in error). However, the stress drop in the Fandoqa earthquake (<3 MPa) [Berberian et al., 2001] was small compared with the mean lithostatic pressure on the back of the wedge (~60 MPa). These relative magnitudes imply that the lithostatic pressure we model is likely to be dominant compared with the deviatoric stresses that can be transmitted across the Fandoqa earthquake fault, supporting the value of the basal shear stress we have calculated.

8. Fault Rheology

Insights into the rheology of the faults can be gained by comparing the stresses and slip rates in the transient postseismic period and during the steady state creep. The change in fault shear stress due to the Fandoqa earthquake was a small proportion (7–20%) of our estimate of the total shear stress driving the steady state creep. However, this change in stress resulted in a significant change in the slip rate on the faults (>500%), shown schematically in Figure 7c. Assuming that there will be no fault motion if there is no driving stress, and that a single rheological law characterizes the fault, a nonlinear relation between the shear stress on the fault and the slip velocity is needed to explain our observations (Figure 7d). If the transient postseismic velocity were higher than the lower bound estimated above, or the tractions on the base of the thrust belt

were greater than those estimated here (e.g., because of an overall tectonic compression related to the motion of the bounding crustal blocks), then the degree of nonlinearity in the relationship between fault stress and sliding velocity would increase.

The Shahdad thrust belt is formed of Neogene molasse-like deposits, thought to be at least 3500 m thick, containing gypsum-rich marls, sandstones, and conglomerates [e.g., *Berberian et al.*, 2001]. These rocks are thought to have been deposited in conditions similar to those on the margin of the thrust belt at the present day, where alluvial fans interfinger with evaporites deposited in ephemeral lakes. Such sediments are likely to form decollement levels, as described by *Bayasgalan et al.* [1999] in Mongolia. Estimating the rheology of the thrusts at Shahdad, which may or may not be lithologically controlled, requires an analysis of the relationship between the driving stresses and deformation rates for a range of possible rheologies. If the motion described here as fault slip were actually the bulk deformation of a weak horizon (e.g., evaporites) within the sedimentary sequence, then the relation between driving stresses and sliding rate would depend upon the deformation mechanism. For diffusion or pressure-solution creep, the layer would act as a Newtonian fluid [e.g., *Evans and Kohlstedt*, 1995] and there would be a linear relationship between shear stress and sliding rate (black dotted line in Figure 7d). This situation is inconsistent with the InSAR results described above unless the deformation is characterized by a yield stress, which is inconsistent with the Newtonian viscous form of diffusion and pressure-solution creep flow laws. If the deformation were by dislocation creep, then the relationship between shear stress and strain rate within the layer can be written $\tau = B\dot{\epsilon}^{1/n}$, where τ is the shear stress, B is a material constant, $\dot{\epsilon}$ is the rate of shear strain, and n is the stress exponent [e.g., *Copley and McKenzie*, 2007]. Experimental results suggest that n has values from 3 to 6 for minerals likely to be capable of dislocation creep at low temperatures (e.g. Halite) [Carter et al., 1993; Franssen, 1994]. For n of 3 to 6, an increase in the shear stress by a factor of 1.2 would lead to an increase in the strain rate by a factor of 1.7 to 3 (pink dotted line in Figure 7d). Such increases are smaller than the size of the velocity increase in the Shahdad thrust belt due to the Fandoqa event (greater than a factor of 5). A stress exponent of ≥ 9 , inconsistent with experimental determinations of the stress exponent for deformation by dislocation creep, would be required to match the observations at Shahdad. These calculations suggest that the observations from Shahdad are inconsistent with the motions being due to bulk shear in a weak layer such as an evaporite horizon.

A nonlinear relationship between stress and slip velocity is also predicated by rate-and-state models for fault friction [e.g., *Dietrich*, 1979; *Ruina*, 1983; *Marone*, 1998]. In these models, the effective coefficient of friction has a logarithmic dependence on the rate of fault motion, and also the evolution of a "state" variable, which describes the evolution of the structural properties of the fault (e.g., the time for which asperities have been in contact). A further parameter gives the critical slip distance by which a fault must slip in order to drive the evolution of the state variable. The equations that describe the rate-and-state friction law are commonly written $\mu = \mu_0 + a \ln(V/V_0) + b \ln(V_0\theta/D_c)$, and $d\theta/dt = 1 - (V\theta/D_c)$, where μ is the coefficient of friction, V is the sliding velocity, θ is the state variable, D_c is the critical slip distance, a and b are constants, and the subscript "0" gives values at a reference sliding velocity. Either of the logarithmic terms in these equations could give rise to a nonlinear relationship between shear stress and sliding velocity, either directly through the term that begins with "a," or indirectly due to the state variable evolving through time due to fault slip, in parallel with the relaxation of the driving stress as the slip accumulates.

A number of studies have suggested that, in situations where changes in slip velocity occur over fault displacements that are considerably larger than D_c , the state dependence of the friction law can be neglected and the behavior is dominated by the rate-dependent term containing "a" [e.g., *Perfettini and Avouac*, 2007; *Barbot et al.*, 2009]. If the laboratory estimates of D_c are used, this assumption is likely to hold true at Shahdad, where displacements of over 10 cm during our time interval of observation are large compared to the commonly suggested values of D_c (e.g., tens of microns) [Marone, 1998]. In this case, the relationship between stress and sliding velocity is given by $\tau = \tau_0 + a\sigma \ln(V/V_0)$, where τ is the shear stress, σ is the effective normal stress, and other symbols are as above. Under this formulation, a change in shear stress would result in a velocity change by a factor of $\exp(\Delta\tau/a\sigma)$. This form of nonlinear relationship between driving stress and sliding velocity is in agreement with the observations from Shahdad (green line in Figure 7d). Using the estimated shear stresses and slip rates described above, the value of a can be estimated as $1.4\text{--}10.4 \times 10^{-3}$. This estimate assumes an effective normal stress equivalent to ambient pressure at a depth of 1 km (with or without hydrostatic pore fluid pressure), and the range in the estimate also encompasses the range in calculated stress changes and slip rates described above. The maximum rate of postseismic slip is not well resolved, so the estimate of

a could be lower than that given here if the maximum postseismic slip rate was faster than the values we estimated above. However, despite the uncertainties in this estimate, it is notable that this value is in the same order of magnitude as laboratory estimates [e.g., Dieterich and Kilgore, 1994; Marone, 1998] and values inferred from some observations of postseismic deformation [e.g., Hearn et al., 2002; Perfettini and Avouac, 2004; Johnson et al., 2006; Barbot et al., 2009; Copley et al., 2012] (if b is assumed to be 0 for the subset of these studies that estimated $(a - b)$). It should be noted that if the fault slip studied here is not large compared with D_c , for example if indirect estimates of D_c based upon earthquake slip are used (e.g., centimeters to meters) [Ohnaka, 2000], then all terms of the rate-and-state friction equations would need to be considered, and the estimate of a presented here would be in error.

A striking feature of the motions we have studied is that the Gowk Fault has ruptured in the Fandoqa earthquake and previous events [Berberian et al., 2001], whereas the adjacent Shahdad fold-thrust belt appears to deform aseismically. A possible explanation for this contrast in behavior lies in the local geology: the Gowk fault cuts through Mesozoic limestones, sandstones, and shales, whereas the Shahdad thrust belt is formed of Neogene sands, conglomerates, and marls [e.g., Geological Survey of Iran, 1992]. Contrasts in the lithology and degree of consolidation between these rocks may explain the different styles of faulting.

Following Berberian et al. [2001] and Fielding et al. [2004], we have interpreted the motions in the Shahdad thrust belt in the interferogram covering the coseismic period, and the first 6 months of postseismic deformation, as postseismic slip. This interpretation is based on the observation that the ratio between fault displacement and the length of the slipped patch on the basal thrust is an order of magnitude lower than seen in earthquakes. If this assumption is wrong, and the motions were coseismic, then our observations have implications for the dynamic propagation of coseismic ruptures onto creeping faults. There are sections of faults that are known to have ruptured coseismically and then undergone postseismic creep [e.g., Copley et al., 2012; Perfettini and Avouac, 2014]. Such a situation is usually interpreted to be the result of dynamic effects during coseismic rupture changing the slip behavior of the faults, and allowing unstable coseismic slip on usually creeping faults [e.g., Noda and Lapusta, 2013]. However, in the known examples the rupture propagation onto the otherwise creeping fault segments involves large amounts of slip (e.g., similar to that on the other parts of the coseismic rupture). In this sense, if the motions seen in the Shahdad thrust belt in Figure 1c were coseismic, then the Fandoqa earthquake would represent a unique case of rupture dynamically propagating for a large distance (>30 km) in response to low levels of slip (~ 8 cm, roughly an order of magnitude lower than on the main coseismic rupture patch). However, we view the more likely explanation of the motions beneath the thrust belt in Figure 1c as being postseismic, which is also consistent with the displacement-to-length ratio of the slip.

9. Conclusions

By estimating the stresses and sliding velocities at separate times within the earthquake cycle on a nearby fault, it has been possible to establish that there is a nonlinear relationship between stress and slip rate on the creeping faults in the thin-skinned Shahdad thrust belt. The degree of nonlinearity is consistent with rate and/or state dependent models of fault friction, but not the bulk deformation of weak layers within the thrust belt by pressure solution, diffusion, or dislocation creep. The overall thrust geometry is a ramp-and-flat system, and creep on the high-angle thrust ramps at the range front is responsible for generating some aspects of the geological and geomorphological structures in the region. However, the folding within the belt must be formed by some combination of ongoing strain that is too slow for us to observe using presently available methods, transient motion due to a driving stress not present in our time of observation, or deformation during the rapid deformation following nearby earthquakes.

Appendix A: Interferograms Used in This Study

Table A1 gives details of the interferograms used in this study. Figure A1 gives standard deviation maps of the two stacks of interferograms shown in Figure 1 in the main paper.

Appendix B: Ascending Track Data

Figure B1 shows a stack of ascending track interferograms (covering a cumulative observation time of 49.0 years; see Table A1 for details of the interferograms used), showing a clear correlation between elevation

Table A1. Details of the Interferograms Used in This Study

Scene 1 Date (yyyymmdd)	Scene 2 Date (yyyymmdd)	Satellite	Track #	Perpendicular Baseline (m)	Duration (years)
Descending track					
<i>pre-earthquake:</i>					
19920529	19960527	ERS 1 and 2	392	−201	4.0
19920807	19960527	ERS 1 and 2	392	−318	3.8
19920911	19960422	ERS 1 and 2	392	74	3.6
19921120	19960527	ERS 1 and 2	392	−152	3.5
<i>co-earthquake and post-earthquake:</i>					
19960422	19990412	ERS2	392	39	3.0
19960527	19980914	ERS2	392	−75	2.3
<i>post-earthquake used in stacks:</i>					
20030630	20091026	Envisat	392	88	6.3
20030630	20091130	Envisat	392	152	6.4
20030908	20090921	Envisat	392	−22	6.0
20031013	20090921	Envisat	392	−130	5.9
20031222	20090817	Envisat	392	58	5.7
20031222	20091026	Envisat	392	−6	5.8
20040126	20090921	Envisat	392	80	5.7
20040719	20090921	Envisat	392	184	5.2
20041101	20090921	Envisat	392	53	4.9
20041206	20090817	Envisat	392	−91	4.7
20041206	20091026	Envisat	392	−155	4.9
<i>post-earthquake not used in stacks:</i>					
19980914	19990308	ERS2	392	−85	0.5
19980914	19990621	ERS2	392	325	0.8
20030630	20031222	Envisat	392	94	0.5
20030630	20040301	Envisat	392	−380	0.7
20030630	20040823	Envisat	392	−74	1.1
20030630	20041206	Envisat	392	243	1.4
20030630	20050530	Envisat	392	33	1.9
20030630	20050808	Envisat	392	−247	2.1
20030908	20031013	Envisat	392	108	0.1
20030908	20040126	Envisat	392	−102	0.4
20030908	20040719	Envisat	392	−206	0.9
20030908	20041206	Envisat	392	−295	1.2
20030908	20050912	Envisat	392	−139	2.0
20031013	20040126	Envisat	392	−210	0.3
20031013	20040405	Envisat	392	316	0.5
20031013	20041101	Envisat	392	−183	1.1
20031013	20050912	Envisat	392	−247	1.9
20031117	20040510	Envisat	392	225	0.5
20031222	20040719	Envisat	392	238	0.6
20031222	20041206	Envisat	392	149	1.0
20031222	20050530	Envisat	392	−61	1.4
20031222	20050912	Envisat	392	305	1.7

Table A1. (continued)

Scene 1 Date (yyyymmdd)	Scene 2 Date (yyyymmdd)	Satellite	Track #	Perpendicular Baseline (m)	Duration (years)
20031222	20091130	Envisat	392	58	5.9
20040126	20040719	Envisat	392	−104	0.5
20040126	20041206	Envisat	392	−193	0.9
20040301	20040510	Envisat	392	−176	0.2
20040301	20040823	Envisat	392	306	0.5
20040301	20050321	Envisat	392	−61	1.1
20040301	20050808	Envisat	392	133	1.4
20040510	20050321	Envisat	392	115	0.9
20040719	20050912	Envisat	392	67	1.1
20040823	20050530	Envisat	392	107	0.8
20040823	20050808	Envisat	392	−173	1.0
20041206	20050530	Envisat	392	−210	0.5
20041206	20091130	Envisat	392	−91	5.0
20050321	20050808	Envisat	392	194	0.4
20050530	20050808	Envisat	392	−280	0.2
20050530	20091026	Envisat	392	55	4.4
20050530	20091130	Envisat	392	119	4.5
20050912	20090817	Envisat	392	−247	3.9
20050912	20090921	Envisat	392	117	4.0
Ascending track					
20030613	20040109	Envisat	156	314	0.6
20040109	20061020	Envisat	156	26	2.8
20040109	20071005	Envisat	156	−28	3.7
20040109	20090522	Envisat	156	−14	5.4
20061020	20071005	Envisat	156	−54	1.0
20061020	20090522	Envisat	156	−40	2.6
20071005	20090522	Envisat	156	14	1.6
20040109	20060113	Envisat	156	213	2.0
20060113	20061020	Envisat	156	−187	0.8
20060113	20070727	Envisat	156	−69	1.5
20070727	20090522	Envisat	156	−158	1.8
20060113	20070622	Envisat	156	−30	1.4
20070622	20090522	Envisat	156	−197	1.9
20040109	20070413	Envisat	156	−167	3.3
20071214	20090522	Envisat	156	117	1.4
20061020	20070413	Envisat	156	−193	0.5
20070413	20071214	Envisat	156	36	0.7
20071005	20071214	Envisat	156	−103	0.2
20070309	20070727	Envisat	156	−57	0.4
20060113	20070309	Envisat	156	−12	1.2
20071109	20090522	Envisat	156	−236	1.5
20070309	20071109	Envisat	156	22	0.7
20061020	20070727	Envisat	156	118	0.8
20030613	20051104	Envisat	156	−52	2.4
20071214	20090417	Envisat	156	138	1.3
20070727	20090626	Envisat	156	−70	1.9

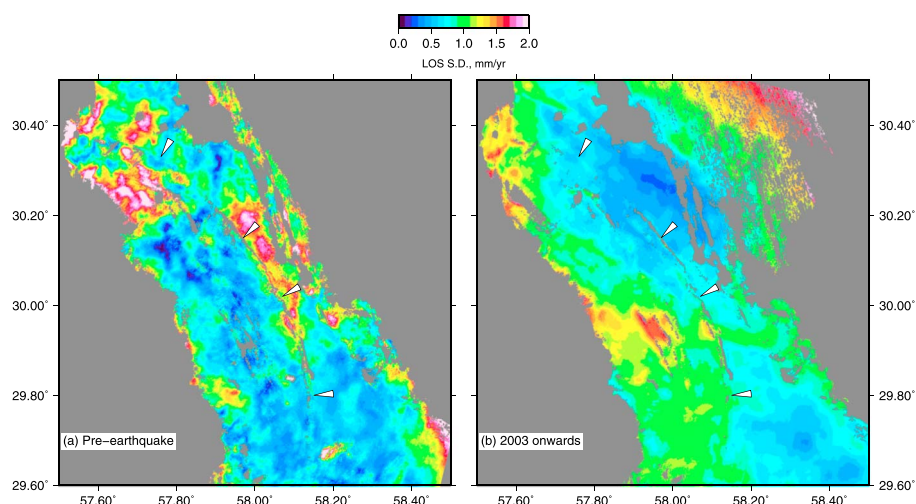
Table A1. (continued)

Scene 1 Date (yyyymmdd)	Scene 2 Date (yyyymmdd)	Satellite	Track #	Perpendicular Baseline (m)	Duration (years)
20061020	20090626	Envisat	156	48	2.7
20051104	20070413	Envisat	156	200	1.4
20071005	20090417	Envisat	156	34	1.5

and signal. This correlation implies the signal is dominated by topographically correlated atmospheric effects. There is enough scatter in the relationship between elevation and phase (Figure B1, bottom) that an empirical relationship between the two is not accurate enough to resolve the small signals studied in the descending track data. Figure B2 shows a network of ascending track interferograms that we have used to construct a time series of displacements, in order to explore if this approach can be used to separate the ground motions from the atmospheric signals. Figure B3 shows the resulting time series, constructed for the same location and using the same methods as the descending track time series discussed in the main paper. The difference in viewing geometry between ascending and descending track acquisitions means that the signal from the fault motion described in the paper will be a factor of ~ 2 smaller in the ascending track data than in the descending track. The dashed grey line shows the resulting prediction for the ascending track time series, based upon the descending track results. This figure shows that the ascending track data are too heavily affected by atmospheric effects for the signals we describe in the descending track data to be visible (i.e., the scatter in the black points is considerably larger than the size of the expected signal, particularly early in the observation period).

Appendix C: Fault Slip Models

The interferogram covering June 2003 to October 2006, used in Figure 5 to constrain the geometry of faulting, is shown in Figure C1. This appendix also contains the inversions for the fault slip and geometry on profiles A–A' (Figure C2) and C–C' (Figure C3). The inversions on profile C–C' were performed on the June 2003 to October 2006 interferogram, as with the inversion on profile B–B' in the main paper. The stack of descending track data has good coherence in the region of profile A–A', and the single interferogram shows an atmospheric artifact in this region (i.e., unlike the rest of the scene, the displacements in this area do not resemble the stacks of data). Therefore, the inversion on profile A–A' was performed on the stack of descending track data shown in Figure 1.


Figure A1. The standard deviation of the stacks of interferograms shown in Figure 1 in the main paper.

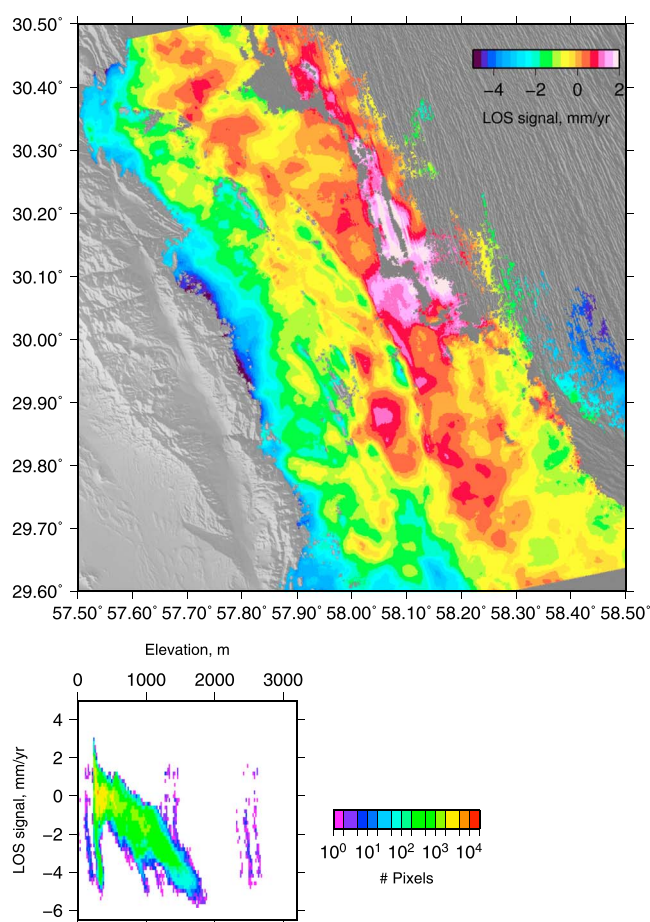


Figure B1. As Figure 1d, but for ascending track data. (top) The apparent rate of line-of-sight motion (note the change in color scale from Figure 1). (bottom) The clear correlation between signal and elevation.

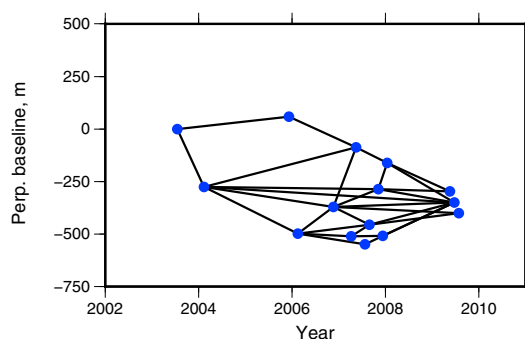


Figure B2. Network of interferograms used for the stack of interferograms shown in Figure B1 and for the time series analysis shown in Figure B3.

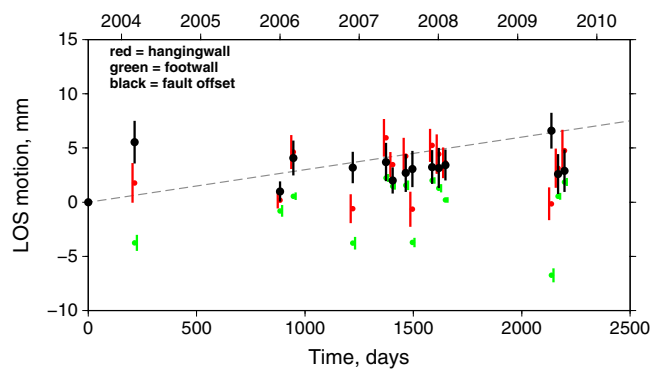


Figure B3. As Figure 4 in the main paper, but produced using the ascending track data shown in Figure B2.

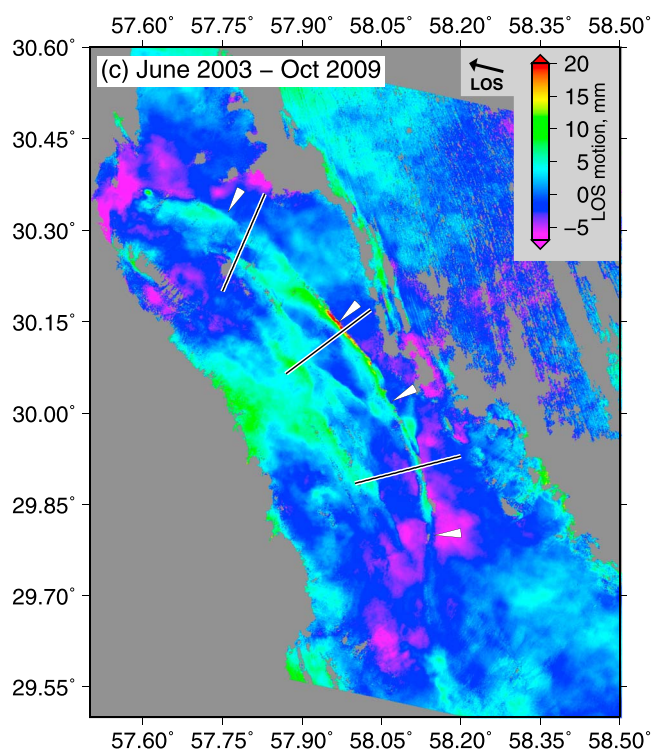


Figure C1. The interferogram covering June 2003 to October 2006, used in Figure 5 to constrain the geometry of faulting.

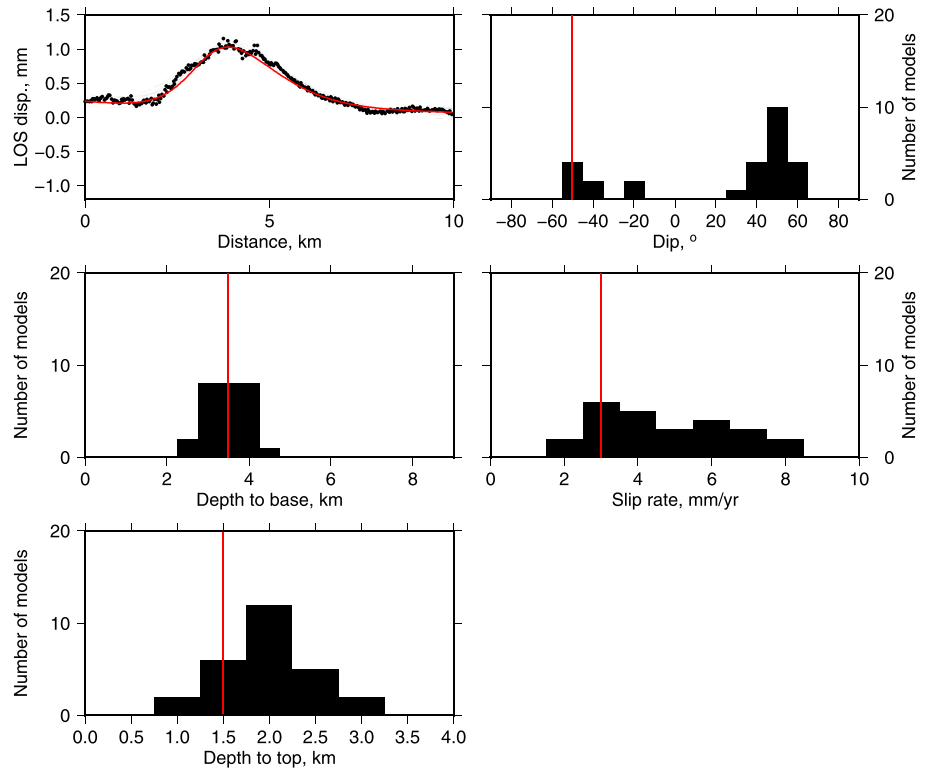


Figure C2. (a) Black circles are displacements in the InSAR line of sight from the stack of interferograms shown in Figure 1d, along the line of profile A–A'. Red line is the best fitting model due to slip on a fault, and grey lines are models that fit the data to within 25% of the minimum misfit. (b) Dips of the faults that fit the data to within 25% of the minimum misfit solution. Positive dips are to the SW, and negative dips are to the NE. The red line shows the best fit solution. (c–e) As Figure C2b, but for the depth to the base of the fault, the slip rate, and the depth to the top of the fault. The fault strike and along-strike length were taken as 25° and 6 km.

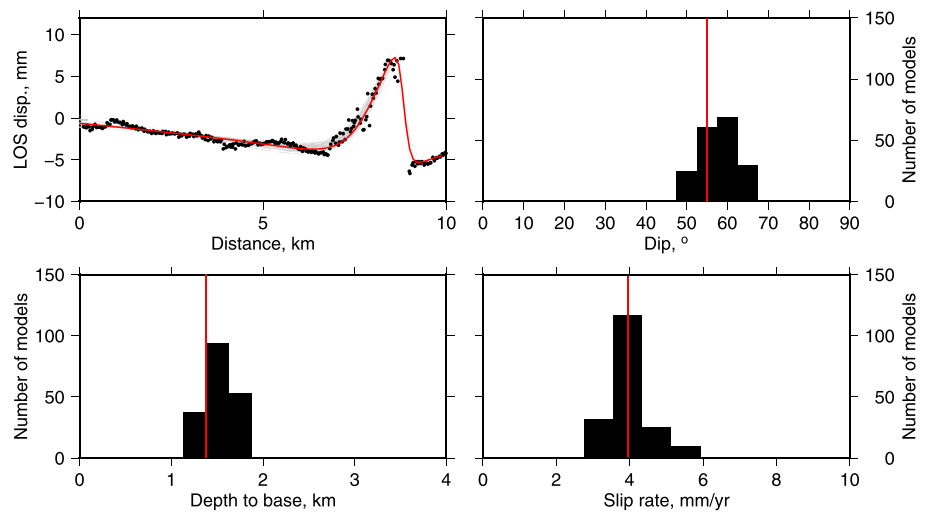


Figure C3. (a) Black circles are displacements in the InSAR line of sight from the interferogram shown in Figure C1, along the line of profile C–C'. Red line is the best fitting model due to slip on a fault, and grey lines are models that fit the data to within 25% of the minimum misfit. (b) Dips of the faults that fit the data to within 25% of the minimum misfit solution. The red line shows the best fit solution. (c and d) As Figure C3b, but for the depth to the base of the fault and the amount of slip (expressed as the average slip rate over the time interval covered by the interferogram). The fault strike and along-strike length were taken as 76° and 6.5 km.

Acknowledgments

We thank James Jackson for the use of his field photographs and for useful discussions. The SAR data used in this study were obtained from the European Space Agency. Our interferograms can be obtained from the corresponding author upon request. The topography data used were the SRTM data set, which is freely available on the internet. R.J. thanks the Marie-Curie ITN "ITECC" for financial support. We thank Gilles Peltzer and two anonymous reviewers for comments that helped improve the manuscript. This work forms part of the NERC- and ESRC-funded project 'Earthquakes without Frontiers', and was partially funded by the NERC grant 'Looking Inside the Continents from Space'.

References

- Barbot, S., Y. Fialko, and Y. Bock (2009), Postseismic deformation due to the Mw 6.0 2004 Parkfield earthquake: Stress-driven creep on a fault with spatially variable rate-and-state friction parameters, *J. Geophys. Res.*, *114*, B07405, doi:10.1029/2008JB005748.
- Bayasgalan, A., J. Jackson, J.-F. Ritz, and S. Carretier (1999), Forebergs, flower structures, and the development of large intra-continental strike-slip faults: The Gurvan Bogd fault system in Mongolia, *J. Struct. Geol.*, *21*, 1285–1302.
- Berberian, M. (1979), Earthquake faulting and bedding thrust associated with the Tabas-e-Golshan (Iran) earthquake of September 16, 1978, *Bull. Seismol. Soc. Am.*, *69*, 1861–1887.
- Berberian, M., J. A. Jackson, E. Fielding, B. E. Parsons, K. Priestley, M. Qorashi, M. Talebian, R. Walker, T. J. Wright, and C. Baker (2001), The 1998 March 14 Fandoqa earthquake (Mw 6.6) in Kerman province, southeast Iran: Re-rupture of the 1981 Sirch earthquake fault, triggering slip on adjacent thrusts and the active tectonics of the Gowk fault zone, *Geophys. J. Int.*, *146*, 371–398.
- Carter, N. L., S. T. Horseman, J. E. Russell, and J. Handin (1993), Rheology of rocksalt, *J. Struct. Geol.*, *15*, 1257–1271.
- Copley, A. (2012), The formation of mountain range curvature by gravitational spreading, *Earth Planet. Sci. Lett.*, *351*–352, 208–214.
- Copley, A. (2014), Postseismic afterslip 30 years after the 1978 Tabas-e-Golshan (Iran) earthquake: Observations and implications for the geological evolution of thrust belts, *Geophys. J. Int.*, *197*, 665–679.
- Copley, A., and D. McKenzie (2007), Models of crustal flow in the India-Asia collision zone, *Geophys. J. Int.*, *169*, 683–698.
- Copley, A., and K. Reynolds (2014), Imaging topographic growth by long-lived postseismic afterslip at Sefidabeh, east Iran, *Tectonics*, *33*, 330–345.
- Copley, A., J. Hollingsworth, and E. Bergman (2012), Constraints on fault and lithosphere rheology from the coseismic slip and postseismic afterslip of the 2006 Mw7.0 Mozambique earthquake, *J. Geophys. Res.*, *117*, B03404, doi:10.1029/2011JB008580.
- Dieterich, J. H., and B. D. Kilgore (1994), Direct observation of frictional contacts: New insights for state-dependent properties, *Pure Appl. Geophys.*, *143*, 283–302.
- Dietrich, W. E. (1979), Modelling of rock friction: 1. Experimental results and constitutive equations, *J. Geophys. Res.*, *84*, 2161–2168.
- Evans, B., and D. L. Kohlstedt (1995), Rheology of rocks, in *Rock Physics and Phase Relations: A Handbook of Physical Constants*, edited by T. J. Ahrens, pp. 148–165, AGU, Washington, D. C., doi:10.1029/RF003p0148.
- Fielding, E. J., T. J. Wright, J. Muller, B. E. Parsons, and R. Walker (2004), Aseismic deformation of a fold-and-thrust belt imaged by synthetic aperture radar interferometry near Shahdad, southeast Iran, *Geology*, *32*, 577–580.
- Franssen, R. C. M. W. (1994), The rheology of synthetic rocksalt in uniaxial compression, *Tectonophysics*, *233*, 1–40.
- Geological Survey of Iran (1992), Kerman quadrangle map.
- Geological Survey of Iran (1993), Bam quadrangle map.
- Hearn, E. H., R. Burgmann, and R. E. Reilinger (2002), Dynamics of Izmit earthquake postseismic deformation and loading of the Duzce earthquake hypocentre, *Bull. Seismol. Soc. Am.*, *92*, 172–193.
- Herman, F., et al. (2010), Exhumation, crustal deformation, and thermal structure of the Nepal Himalaya derived from the inversion of thermochronological and thermobarometric data and modeling of the topography, *J. Geophys. Res.*, *115*, B06407, doi:10.1029/2008JB006126.
- Johnson, K., R. Burgmann, and K. Larson (2006), Frictional properties on the San Andreas Fault near Parkfield, California, inferred from models of afterslip following the 2004 earthquake, *Bull. Seismol. Soc. Am.*, *96*, S321–S338, doi:10.1785/0120050808.
- Jolivet, R., P. S. Agram, N. Y. Lin, M. Simons, M.-P. Doin, G. Peltzer, and Z. Li (2014), Improving InSAR geodesy using global atmospheric models, *J. Geophys. Res. Solid Earth*, *119*, 2324–2341, doi:10.1002/2013JB010588.
- Kaneko, Y., Y. Fialko, D. T. Sandwell, X. Tong, and M. Furuya (2013), Interseismic deformation and creep along the central section of the North Anatolian Fault (Turkey): InSAR observations and implications for rate-and-state friction properties, *J. Geophys. Res. Solid Earth*, *118*, 316–331, doi:10.1029/2012JB009661.
- Lamb, S. (2006), Shear stresses on megathrusts: Implications for mountain building behind subduction zones, *J. Geophys. Res.*, *111*, B07401, doi:10.1029/2005JB003916.
- Marone, C. (1998), The effect of loading rate on static friction and the rate of fault healing during the earthquake cycle, *Nature*, *391*, 69–72.
- Noda, H., and N. Lapusta (2013), Stable creeping fault segments can become destructive as a result of dynamic weakening, *Nature*, *493*, 518–521.
- Ohnaka, M. (2000), A physical scaling relation between the size of an earthquake and its nucleation size, *Pure Appl. Geophys.*, *157*, 2259–2282.
- Okada, Y. (1985), Surface deformation due to shear and tensile faults in a half-space, *Bull. Seismol. Soc. Am.*, *75*(4), 1135–1154.
- Perfettini, H., and J.-P. Avouac (2004), Postseismic relaxation driven by brittle creep: A possible mechanism to reconcile geodetic measurements and the decay rate of aftershocks, application to the Chi-Chi earthquake, Taiwan, *J. Geophys. Res.*, *109*, B02304, doi:10.1029/2003JB002488.
- Perfettini, H., and J.-P. Avouac (2007), Modeling afterslip and aftershocks following the 1992 Landers earthquake, *J. Geophys. Res.*, *112*, B07409, doi:10.1029/2006JB004399.
- Perfettini, H., and J.-P. Avouac (2014), The seismic cycle in the area of the 2011 Mw9.0 Tohoku-Oki earthquake, *J. Geophys. Res. Solid Earth*, *119*, 4469–4515, doi:10.1002/2013JB010697.
- Reynolds, K., A. Copley, and E. Hussain (2015), Evolution and dynamics of a fold-thrust belt: The Sulaiman Range of Pakistan, *Geophys. J. Int.*, *201*, 683–710.
- Ruina, A. (1983), Slip instability and state variable friction laws, *J. Geophys. Res.*, *88*, 10,359–10,370.
- Scholz, C. H. (1998), Earthquakes and friction laws, *Nature*, *391*, 37–42.
- Suppe, J. (2007), Absolute fault and crustal strength from wedge tapers, *Geology*, *35*, 1127–1130.
- Usai, S. (2003), A least squares database approach for SAR interferometric data, *IEEE Trans. Geosci. Remote Sens.*, *41*, 753–760.
- Walker, R., and J. Jackson (2002), Offset and evolution of the Gowk fault, SE Iran: A major intra-continental strike-slip system, *J. Struct. Geol.*, *24*, 1677–1698.
- Walker, R., J. Jackson, and C. Baker (2003), Surface expression of thrust faulting in eastern Iran: Source parameters and surface deformation of the 1978 Tabas and 1968 Ferdows earthquake sequences, *Geophys. J. Int.*, *152*, 749–765.
- Walpersdorf, A., et al. (2014), Present-day kinematics and fault slip rates in eastern Iran, derived from 11 years of GPS data, *J. Geophys. Res. Solid Earth*, *119*, 1359–1383, doi:10.1002/2013JB010620.